11-1995

Aliasing Reduction in Staring Infrared Imagers Utilizing Subpixel Techniques

Joseph C. Gillette
Technology/Scientific Services Inc.

Thomas M. Stadtmiller
Technology/Scientific Services Inc.

Russell C. Hardie
University of Dayton, rhardie1@udayton.edu

Aliasing reduction in staring infrared imagers utilizing subpixel techniques

Joseph C. Gillette
Thomas M. Stadtmiller
Technology/Scientific Services, Inc.
WL/AARI-3 Building 622
3109 P Street
Wright Patterson Air Force Base, Ohio 45433-7700
E-mail: gillette@goofy.aa.wpafb.af.mil

Russell C. Hardie
University of Dayton
300 College Park
Dayton, Ohio 45469-0226
E-mail: rhardie@engr.udayton.edu

Abstract. We introduce and analyze techniques for the reduction of aliased signal energy in a staring infrared imaging system. A standard staring system uses a fixed two-dimensional detector array that corresponds to a fixed spatial sampling frequency determined by the detector pitch or spacing. Aliasing will occur when sampling a scene containing spatial frequencies exceeding half the sampling frequency. This aliasing can significantly degrade the image quality. The aliasing reduction schemes presented here, referred to as microscanning, exploit subpixel shifts between time frames of an image sequence. These multiple images are used to reconstruct a single frame with reduced aliasing. If the shifts are controlled, using a mirror or beam steerer for example, one can obtain a uniformly sampled microscanned image. The reconstruction in this case can be accomplished by a straightforward interlacing of the time frames. If the shifts are uncontrolled, the effective sampling may be nonuniform and reconstruction becomes more complex. A sampling model is developed and the aliased signal energy is analyzed for the microscanning techniques. Finally, a number of experimental results are presented that illustrate the performance of the microscanning methods.

Subject terms: microscanning; aliasing; high resolution; subpixel; infrared imaging; motion estimation.

Optical Engineering 34(11), 3130–3137 (November 1995).

1 Introduction

Image acquisition using an infrared (IR) sensor is susceptible to a variety of degradation processes. Imperfect optics, finite detector arrays, and finite individual detector sizes all contribute to the nonideal sampling of the scene information. The problem addressed in this paper is that of insufficient sample rate. A standard staring IR system uses a fixed two-dimensional detector array, which corresponds to a fixed spatial sampling frequency determined by the detector pitch or spacing. The Nyquist theorem dictates that aliasing will occur when sampling a scene containing spatial frequencies exceeding half this sampling frequency. Most natural scenes are not bandlimited, and the aliasing resulting from undersampling can significantly degrade the quality and utility of the image.

In this paper, we introduce and analyze techniques to reduce the aliased signal energy in a staring infrared imaging system and significantly improve the image quality. The algorithms proposed use multiple undersampled time frames of a stationary scene to estimate a single high-resolution image. The techniques rely on subpixel shifts between the time frames such that each time frame can provide unique samples of the scene. By properly combining the set of shifted images, an image effectively sampled at a higher rate than the individual frames can be obtained. This process is referred to as microscanning.[1]

The microscanning techniques presented here are divided into the categories of controlled and uncontrolled. For controlled microscanning, the relative subpixel shifts between image frames are produced intentionally. This can be accomplished using a microscan mirror or beam steerer, for example. With control over the shifts, a set of images can be generated so as to form a uniform high-resolution grid. Thus, the high-resolution image is generated by a straightforward interlacing of the undersampled image frames. In an uncontrolled microscanning case, shifts between the frames are uncontrolled and are generally unknown *a priori*. Such shifts may occur as the result of random motion between the scene and the focal plane from either vibration or camera panning. Thus, the resulting sampling of the scene may be nonuniform, and the high-resolution reconstruction becomes more complex. While the controlled microscanning technique has been analyzed previously, the uncontrolled microscanning technique proposed here is novel. Another technique for high-resolution image reconstruction has been proposed by Kim et al.[2] using a weighted recursive least-squares algorithm. The algorithm proposed in our paper offers greater computational simplicity and lends itself to real-time implementation.

This paper is organized as follows. In Sec. 2, we develop a theoretical model for the nonideal sampling of the staring array imager as well as a figure of merit for aliased signal

Paper RS-014 received Mar. 31, 1995; revised manuscript received June 1, 1995; accepted for publication June 19, 1995.

energy. Section 3 describes microscanning in the controlled and uncontrolled cases. An analysis of aliased signal energy using microscanning is also developed. In Sec. 4, a number of experimental results are presented that illustrate the performance of the microscanning techniques on real imagery. Finally, some conclusions are given in Sec. 5.

2 Sampling Theory

Before describing microscanning, some background on sampling theory in an imaging system is reviewed. In Sec. 2.1, nonideal sampling is discussed, and the effects of the optics, sampling array size, and detectors in real sampling are modeled. In Sec. 2.2, a figure of merit for aliased energy is developed.

2.1 *Nonideal Sampling in a Staring Array*

In a staring array, sampling is performed by a finite array of detectors, which must integrate incident photon flux collected through an optical system. Thus, there are three main considerations in the model: the optics, the detector charge integration, and the finite-size detector array.

The block diagram in Fig. 1 illustrates the sampling process in a staring array. First, consider the optics. The point spread function of the optics, denoted psf(x,y), modifies the object scene, $o(x,y)$, so that

$$f(x,y)=\mathrm{psf}(x,y)*o(x,y)\ . \tag{1}$$

The optical transfer function OTF$(\cdot)$ is the Fourier transform of psf$(\cdot)$. Since psf$(\cdot)$ is infinite in extent, OTF$(\cdot)$ effectively bandlimits the input scene, as higher spatial frequencies cannot enter the optics pupil.[3,4] However, this may not be sufficient to prevent aliasing.

Next, consider the integration of charge over each detector. The object scene incident on the detector array is continuous and must be sampled and quantized. The incident photons on the individual detectors are essentially averaged over the area of the detector.[10] This integration can be written as

$$\begin{aligned} f_i(x,y)&=\int_{-\infty}^{\infty}\int_{-\infty}^{\infty} f(\nu,\lambda)d(x-\nu,y-\lambda)\ \mathrm{d}\lambda\ \mathrm{d}\nu \\ &=f(x,y)*d(x,y)\ , \end{aligned} \tag{2}$$

where $d(\cdot)$ is determined by the detector geometry. This result is limited by the extent of the detector array. The limiting function is expressed as $r(\cdot)$ and, when applied to $f_i(x,y)$, results in

$$f_r(x,y)=f_i(x,y)r(x,y)\ . \tag{3}$$

To apply this integration to all of the detectors, it is multiplied by the sampling lattice, yielding

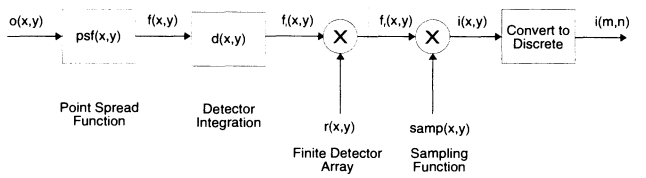

Fig. 1 Basic block diagram of the imaging system.

$$i(x,y)=f_r(x,y)\ \mathrm{samp}_{\Delta x,\Delta y}(x,y)\ , \tag{4}$$

where

$$\begin{aligned} \mathrm{samp}_{\Delta x,\Delta y}(x,y)&=\frac{1}{\Delta x\ \Delta y}\sum_{m=-\infty}^{\infty}\sum_{n=-\infty}^{\infty}\delta\left(\frac{x}{\Delta x}-m,\frac{y}{\Delta y}-n\right) \\ &=\sum_{m=-\infty}^{\infty}\sum_{n=-\infty}^{\infty}\delta(x-m\Delta x,y-n\Delta y)\ . \end{aligned} \tag{5}$$

Combining Eqs. (1), (2), (3), and (4) results in

$$i(x,y)=[o(x,y)*\mathrm{psf}(x,y)*d(x,y)]r(x,y)\ \mathrm{samp}_{\Delta x,\Delta y}(x,y) \tag{6}$$

in the spatial domain and

$$\begin{aligned} I(\xi_1,\xi_2)=&[O(\xi_1,\xi_2)\ \mathrm{OTF}(\xi_1,\xi_2)\ D(\xi_1,\xi_2)]*R(\xi_1,\xi_2) \\ &*\mathrm{SAMP}_{\xi_1^s,\xi_2^s}(\xi_1,\xi_2) \end{aligned} \tag{7}$$

in the frequency domain, where

$$R(\xi_1,\xi_2)=\Im\{r(x,y)\}\ , \tag{8}$$

$$D(\xi_1,\xi_2)=\Im\{d(x,y)\}\ , \tag{9}$$

and

$$\begin{aligned} \mathrm{SAMP}_{\xi_1^s,\xi_2^s}(\xi_1,\xi_2)&=\Im\{\mathrm{samp}(x,y)\} \\ &=\frac{1}{\Delta x\ \Delta y}\sum_{m=-\infty}^{\infty}\sum_{n=-\infty}^{\infty}\delta\left(\xi_1-\frac{m}{\Delta x},\ \xi_2-\frac{n}{\Delta y}\right) \\ &=\xi_1^s\xi_2^s\sum_{m=-\infty}^{\infty}\sum_{n=-\infty}^{\infty}\delta(\xi_1-m\xi_1^s,\ \xi_2-n\xi_2^s)\ . \end{aligned} \tag{10}$$

The operator $\Im\{\cdot\}$ represents the continuous Fourier transform.

Equations (6) and (7) are the results for the general case, and the functions $d(\cdot)$ and $r(\cdot)$ can represent any geometry. However, for our imaging system, the effects due to the detector integration will be defined as

$$d(x,y)=\frac{1}{|ab|}\ \mathrm{rect}\left(\frac{x}{a},\frac{y}{b}\right)\ , \tag{11}$$

where a and b are the dimensions of the individual detectors. The detector array is also rectangular, so that

$$r(x,y)=\mathrm{rect}\left(\frac{x}{X},\frac{y}{Y}\right)\ , \tag{12}$$

where X and Y are the dimensions of the detector array. The frequency-domain representations for each of these functions are

$$D(\xi_1,\xi_2)=\mathrm{sinc}(a\xi_1,b\xi_2) \tag{13}$$

and

$$R(\xi_1,\xi_2) = XY\ \mathrm{sinc}(X\xi_1, Y\xi_2)\ . \tag{14}$$

An illustration of the detector array is shown in Fig. 2.

The last block in Fig. 1 represents the conversion of $i(x,y)$, which contains only Dirac delta functions, to a discrete sequence $i(m,n)$.

The following section develops a measure of aliasing distortion and resolution degradation as a function of the sampling frequency.

2.2 *Aliased Signal Energy*

A quantitative measure of the benefits of microscanning is important for objective evaluation. To begin, consider Eq. (7) rewritten as

$$I(\xi_1,\xi_2) = O(\xi_1,\xi_2)H_{\mathrm{pre}}(\xi_1,\xi_2) * \mathrm{SAMP}_{\xi_1^s,\xi_2^s}(\xi_1,\xi_2)\ , \tag{15}$$

where $H_{\mathrm{pre}}(\xi_1,\xi_2)$ can be thought of as a presampling filter and is given by

$$H_{\mathrm{pre}}(\xi_1,\xi_2) = [\mathrm{OTF}(\xi_1,\xi_2)\ D(\xi_1,\xi_2)] * XY\ \mathrm{sinc}(X\xi_1, Y\xi_2)\ . \tag{16}$$

An ideal low-pass "boxcar" filter with cutoffs of $\xi_1^s/2$ and $\xi_2^s/2$ is desired here; however, due to the nonideal elements in the optics and sampling process, this cannot be implemented. The spectrum just before the sampler is given by

$$F_{\mathrm{pre}}(\xi_1,\xi_2) = O(\xi_1,\xi_2)H_{\mathrm{pre}}(\xi_1,\xi_2)\ . \tag{17}$$

The total signal energy is given by

$$E_{\mathrm{pre}}^{\mathrm{total}} = \int_{-\infty}^{\infty}\int_{-\infty}^{\infty} |F_{\mathrm{pre}}(\xi_1,\xi_2)|^2\ \mathrm{d}\xi_1\ \mathrm{d}\xi_2\ , \tag{18}$$

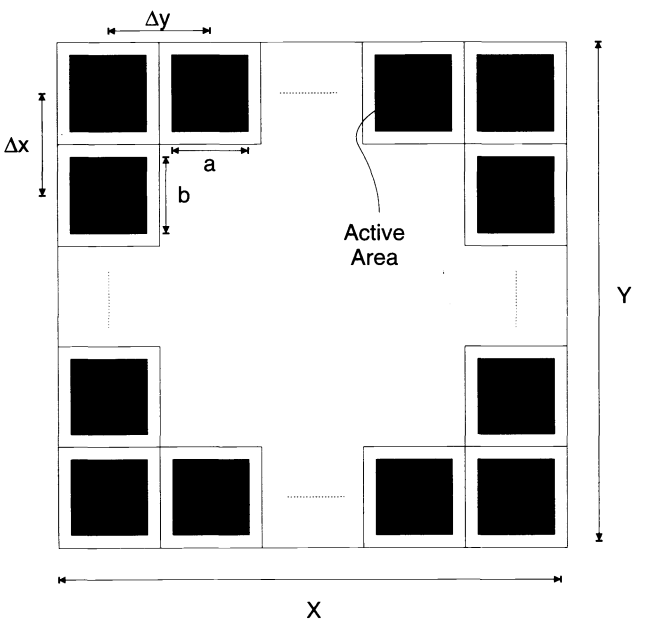

Fig. 2 Detector array. Notice that the active detector width is less than the sampling pitch in both dimensions.

where $|F_{\mathrm{pre}}(\xi_1,\xi_2)|^2$ is the energy spectral density (ESD) of the filtered object scene.

Next, consider an ideal reconstruction filter,

$$H_R^{\mathrm{ideal}}(\xi_1,\xi_2) = \begin{cases} 1, & |\xi_1| < \xi_1^s/2\ \ |\xi_2| < \xi_2^s/2 \\ 0 & \text{otherwise.} \end{cases} \tag{19}$$

The signal energy after the reconstruction filter is given by

$$E_R = \int_{-\infty}^{\infty}\int_{-\infty}^{\infty} |F_{\mathrm{pre}}(\xi_1,\xi_2)H_R^{\mathrm{ideal}}(\xi_1,\xi_2)|^2\ \mathrm{d}\xi_1\ \mathrm{d}\xi_2 = \int_{-\xi_1^s/2}^{\xi_1^s/2}\int_{-\xi_2^s/2}^{\xi_2^s/2} |F_{\mathrm{pre}}(\xi_1\xi_2)|^2\ \mathrm{d}\xi_1\ \mathrm{d}\xi_2\ . \tag{20}$$

The signal energy outside the passband of $H_R^{\mathrm{ideal}}(\xi_1,\xi_2)$ will be folded over in the sampled signal spectrum as aliased energy. This can be rephrased simply: all energy at frequencies greater than half the sampling frequency is considered aliased energy. This aliased energy can be expressed as

$$E_a = E_{\mathrm{pre}}^{\mathrm{total}} - E_R\ . \tag{21}$$

The aliasing error[5] can be defined as the ratio of the aliased energy to the total energy in the reconstructed spectrum, or

$$\zeta_a = \frac{E_a}{E_R}\ . \tag{22}$$

The ratio of signal to aliasing noise energy, denoted SNR_a, is given by

$$\mathrm{SNR}_a = \frac{E_R}{E_a} = \frac{1}{\zeta_a}\ . \tag{23}$$

In the same manner, a measure of image-resolution degradation can be defined.[5] This effect is due to the presampling filter. The energy of the object scene can be expressed as

$$E_O = \int_{-\xi_1^s/2}^{\xi_1^s/2}\int_{-\xi_2^s/2}^{\xi_2^s/2} |O(\xi_1,\xi_2)|^2\ \mathrm{d}\xi_1\ \mathrm{d}\xi_2\ , \tag{24}$$

where $|O(\xi_1,\xi_2)|^2$ is the energy spectral density of the object scene. The resolution error due to the presampling filter is defined as

$$\zeta_R = \frac{E_O - E_R}{E_O}\ . \tag{25}$$

The error values ζ_R and ζ_a will vary with different sampling frequencies, optics, and detector arrays. The figure of merit SNR_a is used to evaluate the microscanning techniques. Note that resolution error is not decreased with sampling frequency. The resolution error relates only to the difference between the input signal and the output of the presampling filter. Thus, it may increase with higher sampling rates. An inverse filter can be used to attempt to remove the effects of the presampling filter.

3 Microscanning Theory

This section describes both controlled and uncontrolled mi-

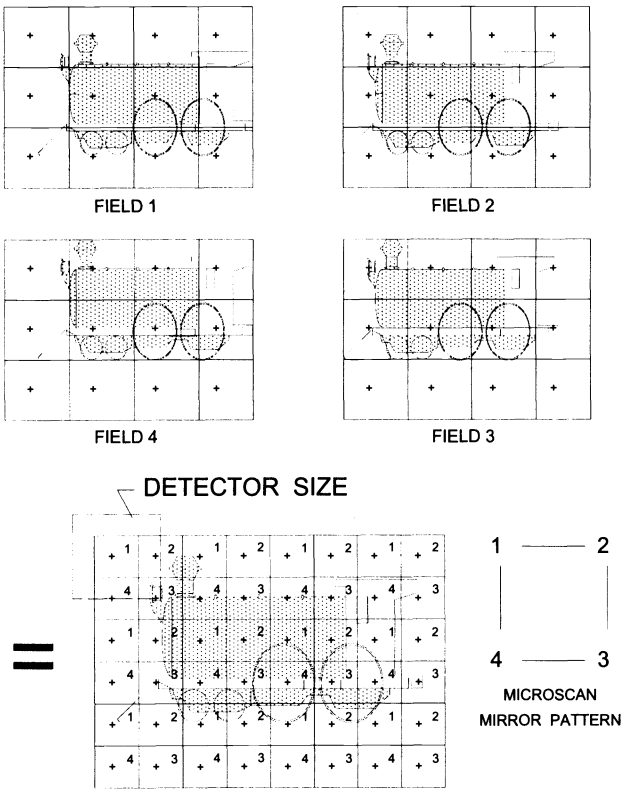

Fig. 3 Illustration of a level-2 microscanning process. The individual images are shifted by half pixels for four separate positions. The reconstructed image has four times as many unique samples as any of the four fields.

croscanning to reduce image aliasing. Specifically, Sec. 3.1 describes controlled microscanning and provides an analysis of the aliased image energy in a specific example. Section 3.2 develops the uncontrolled microscanning technique.

3.1 *Controlled Microscanning*

Controlled microscanning implies that the subpixel shifts between temporal image frames are controlled and are therefore known *a priori.* Furthermore, these shifts are generally selected to produce a set of images that fall onto a uniform grid. We define a level $=L$ microscan to be one where L^2 frames are imaged and each frame has its own unique controlled subpixel shift, each shift being part of a uniform grid. This means that each frame has a relative pixel shift that is an integer multiple of $1/L$. The shifted images are simply interlaced on the uniform grid to form a high-resolution microscanned image. Since no processing of the images is required, controlled microscanning can readily be implemented in real time. An example of a level-2 microscan is depicted in Fig. 3.

Watson et al.[1] have developed a sampling model for a level-2 microscan. This model introduces additional shifted sampling functions, resulting from a shift of the object on the detector array. Here we extend this result to a level-L microscan. To do this, consider the model of the sampled image from (6), ignoring the effect of the finite detector array:

$$i_s(x,y) = [d(x,y) * o(x,y) * \mathrm{psf}(x,y)]\ \mathrm{samp}_{\Delta x,\Delta y}(x,y)\ . \tag{26}$$

The effect of the finite detector array will be small compared to the effects of the detector integration and psf(x,y). It is clear that with the fixed sampling function, the sampling frequencies are also fixed. The level-L microscanned image can be modeled as

$$i_{\mathrm{ms}}^{L}(x,y) = [d(x,y) * o(x,y) * \mathrm{psf}(x,y)] \cdot \frac{1}{L^2}\sum_{i=0}^{L-1}\sum_{j=0}^{L-1}\mathrm{samp}_{\Delta x,\Delta y}\left(x-\frac{i}{L},\ y-\frac{j}{L}\right)$$
$$= [d(x,y) * o(x,y) * \mathrm{psf}(x,y)]\,\mathrm{samp}_{\Delta x/L,\ \Delta y/L}(x,y)\ . \tag{27}$$

The basic assumption is that the object and the imaging system remain constant during the acquisition of the multiple frames. Taking the Fourier transform of (27) yields the spatial frequency spectrum of the microscanned image,

$$I_{\mathrm{ms}}^{L}(\xi_1,\xi_2) = [D(\xi_1,\xi_2)O(\xi_1,\xi_2)\ \mathrm{OTF}(\xi_1,\xi_2)] * \mathrm{SAMP}_{L\xi_1^s,L\xi_2^s}(\xi_1,\xi_2)\ . \tag{28}$$

Thus, level-L microscanning effectively increases the sampling rate by L without changing the detector size or spacing. This will, in turn, reduce aliasing.

Example 1 illustrates the effect of controlled microscanning on ζ_a, ζ_R, and SNR_a for a specific imaging system.

Example 1 (Aliasing and resolution error). Consider an imager having $f/3$ 100-mm optics, a detector pitch of 50 μm ($\Delta x = \Delta y = 50$ μm), and an active detector area of 40 μm $\times$ 40 μm operating at a wavelength of 4 μm (the center of the midwavelength IR spectrum). The sampling frequency is 2 cycles/mrad, and, neglecting the finite extent of the detector array, the signal will be bandlimited to the OTF cutoff of 8.33 cycles/mrad. Because of the sampling frequency, any signal energy above a frequency of 1 cycle/mrad will be aliased.

Now, consider light from a point source entering the imaging system. The ESD of the prefiltered point source is given by

$$|F_{\mathrm{pre}}(\xi_1,\xi_2)|^2 = |\mathrm{OTF}(\xi_1,\xi_2)\ D(\xi_1,\xi_2)|^2\ . \tag{29}$$

The 1-D magnitude response of OTF$(\cdot)$, or the modulation transfer function MTF$(\cdot)$, for the system used here is shown in Fig. 4. This response is a theoretical result based upon system parameters and the assumption is that there are no obscurations or aberrations.[3,4] Also shown in Fig. 4 are $D(\xi_1)$ and the ESD of the prefiltered point source.

Note that for a level-L microscan, the aliased energy is given by the area under the ESD for frequencies greater than L cycles/mrad and less than $-L$ cycles/mrad. Table 1 records the theoretical results of the resolution degradation and aliasing errors for various microscan levels.

A plot of the SNR_a results in Table 1 can be seen in Fig. 5. As the microscan level increases, the sampling frequency

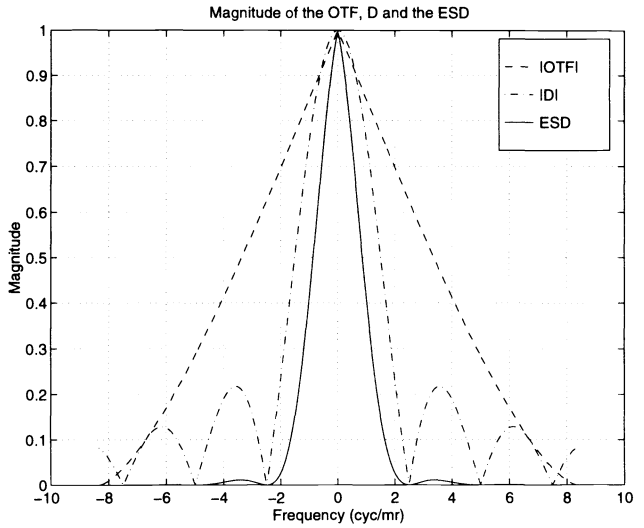

Fig. 4 The magnitudes of OTF(·), the detector transfer function $D(\cdot)$, and the ESD of the prefiltered points source.

Table 1 Theoretical results for the resolution and aliasing errors as well as the aliasing signal-to-noise ratio.

Microscan Level (L)	ζ_R	ζ_A	SNR_a (dB)
1	0.5741	0.2068	15.7
2	0.7699	0.0186	39.8
3	0.8462	0.0127	43.6
4	0.8846	0.0026	59.5
5	0.8893	5.68e-4	74.7
6	0.8893	2.28e-4	83.8
7	0.8893	3.35e-6	126.1
8	0.8893	2.89e-8	173.5

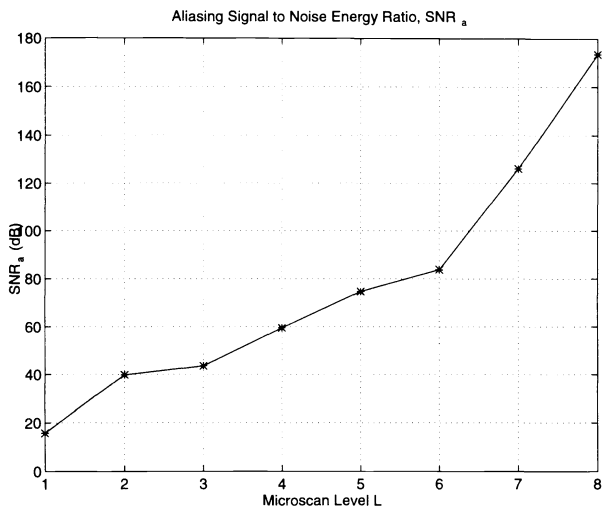

Fig. 5 Aliasing signal-to-noise energy ratio as a function of microscan level.

Table 2 The block matching algorithm.

Block Matching Algorithm
Step 1: Select block of size M x N from the current frame.
Step 2: Find the whole-pixel motion vector by minimizing the MAE between this block and corresponding blocks in the next sequential frame.
Step 3: Expand the block from Step 1 and the block from Step 2 which resulted in the minimum MAE using a spatial interpolator.
Step 4: Repeat Step 1 and Step 2 using the expanded blocks as the new images to find the subpixel motion vector.
Step 5: Add the whole pixel motion vector from Step 2 and the subpixel motion vector from Step 4 to find the estimated motion vector.
Step 6: Repeat Steps 1-5 for p blocks. The final estimated motion vector is the average of the p motion estimates.

increases accordingly, thus reducing aliasing. Since the OTF cuts off at 8.33 cycles/mrad, a level-9 microscan (sampling frequency of 18 cycles/mrad) will *eliminate* aliasing. Note that there is only a 3.8-dB improvement from level 2 to level 3, due to the shape of the ESD in Fig. 4. Also note that the resolution error ζ_R increases as the micrsocan level increases. This is due to a relative decrease in E_R with respect to E_O as the sampling frequency increases.

3.2 *Uncontrolled Microscanning*

Controlled microscanning systems mechanically shift the field-of-view (FOV) of the imagers optical system in $1/L$ increments. In reality, additional shifts may be present due to motion and vibration of the imager's platform. If these shifts become large enough, then the reconstructed microscanned image becomes degraded. In such cases, it may be beneficial to estimate the shifts between the sequential frames and use these estimates to reconstruct the high-resolution microscanned image. Furthermore, using random shifts alone may eliminate the need for the microscan mirror and driver system. Sections 3.2.1 and 3.2.2 introduce a motion estimation technique and high-resolution reconstruction technique for uncontrolled microscanning, respectively.

3.2.1 *Block matching*

Estimating the subpixel shifts that occur between successive frames is the first step in producing a high-resolution image from the low-resolution images. These subpixel shifts can be estimated using the block matching algorithm (BMA).[6–8] The BMA, summarized in Table 2, estimates the displacement vector by comparing the gray-scale values of successive frames on a block-by-block basis. First a template is defined by selecting a block $\tilde{i}_k(m,n)$ of size $M \times N$ from the k'th frame $i_k(m,n)$. A motion vector can then be estimated by scanning the template through a search area in the next sequential frame. The size of the search area can be expressed as $(M+2P)\times(N+2P)$, where P represents the maximum whole pixel shift. At each position in the search area, the mean absolute error (MAE) between the template and the overlapping block is calculated as

$$\mathrm{MAE}(p_m,p_n)=\sum_{m=1}^{M}\sum_{n=1}^{N}|\tilde{i}_k(m,n)-\tilde{i}_{k+1}(m+p_m,\ n+p_n)|$$

$$(-P\leq p_m,p_n\leq P)\ . \qquad (30)$$

The position (p_m,p_n) at which the MAE is a minimum provides an estimate of the nearest whole pixel shift. Once the integer pixel shift is found, subpixel accuracy can be achieved

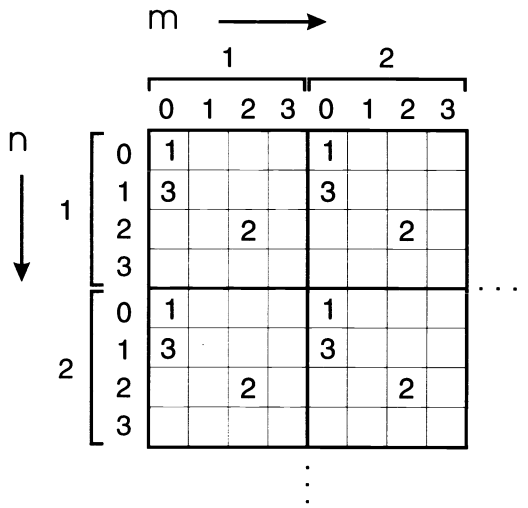

Fig. 6 Illustration of 4×4 high-resolution reconstruction. Image 1 is placed in bin (0,0). Image 2, with a shift of (½,½) of a pixel, is placed in bin (2,2). Image 3, with a shift of (0,¼), is placed in (0,1).

by applying spatial interpolation to the template and the block that resulted in the minimum MAE. The precision to which the shifts can be estimated is determined by the number of interpolation points in between the original data points. The fractional part of the motion vector can then be determined by minimizing the MAE over the finer sampling grid. The estimated motion vector is found by summing the integer and the fractional motion vectors.

A number of factors, including block selection, block size, and the number of estimated shifts to average over, affect the performance of the BMA. For best performance, the selected blocks should contain scene detail such as edges to estimate the shifts between the two frames. The BMA tends to perform poorly in areas with little or no detail. Also, since we are measuring shifts in both the horizontal and vertical directions, edges or scene detail must span in both directions. To ensure good block selection, we propose using only those blocks that result in maximum values of

$$\frac{1}{MN}\sum_{m=1}^{M}\sum_{n=1}^{N}\left[\frac{\tilde{i}(m+1,n)-\tilde{i}(m-1,n)}{2}\right]\cdot\left[\frac{\tilde{i}(m,n+1)-\tilde{i}(m,n-1)}{2}\right]. \tag{31}$$

Choosing the top s blocks will ensure that each selected block has contrast in both the horizontal and vertical directions. A final motion vector is obtained by averaging the s shift estimates.

3.2.2 *High-resolution image reconstruction*

Given accurate frame-to-frame shift estimates from sequential undersampled frames, a higher-resolution image can be constructed. This is done by mapping the lower-resolution images onto a single high-resolution grid according to the estimated interframe displacements. The first frame in an image sequence is mapped onto the (0,0) position of the $L\times L$ high-resolution grid (see Fig. 6). The successive frames are then mapped into the appropriate "bins" according to the estimated shift. An example of a 4×4 high-resolution microscan is illustrated in Fig. 6. Frame 1 is placed in bin (0,0). Frame 2 is placed in bin (2,2), resulting from a shift of (½,½). Frame 3 is placed in bin (0,1), resulting from a shift of (0,¼). This process is continued until each of the bins is filled. If the estimated shift for multiple frames is the same, then the values at those positions can be averaged for noise suppression. If empty bins are present, an interpolation algorithm must be implemented. The computationally simplest method is a nearest-neighbor interpolation algorithm. This will fill the empty bin with the closest neighboring pixel value. Table 3 summarizes the uncontrolled microscanning process.

Table 3 High-resolution reconstruction algorithm.

High Resolution Reconstruction Algorithm
Step 1: Expand the first frame by interlacing it with rows and columns of zeros, thus creating the high resolution grid.
Step 2: Interlace the sequential frames based upon their measured shift from the BMA.
Step 3: Average frames landing in the same bins for noise suppression.
Step 4: Interpolate to fill empty bins and complete the high resolution image.

This reconstruction method is desirable because of its computational simplicity. A high-resolution image with decreased aliasing can be constructed quickly with few operations, and therefore lends itself to real-time implementation.

4 Experimental Results

In this section, experimental results illustrating the performance of controlled microscanning, the BMA, and the high-resolution reconstruction algorithm are presented.

4.1 *Controlled Microscanning*

A controlled microscan was performed on a spoke target using the variable parameter forward-looking infrared (VPFLIR) testbed.[9] A single-frame midwave (3 to 5 μm) IR image of size 128×128, expanded to 256×256 using pixel replication, is shown in Fig. 7(a). Pixel replication has been used to facilitate comparison with the microscanned image. The 2×2 controlled microscanned image is shown in Fig. 7(b). Notice how the aliasing is reduced and how much further towards the center of the target the spokes extend before being distorted.

4.2 *Block Matching Algorithm*

In order to test the BMA and high-resolution reconstruction algorithm, a 4×4 microscan mirror pattern has been programmed, which shifts the image in ¼-pixel increments in both the horizontal and vertical directions. A total of sixteen 64×64 staring images have been recorded in this fashion. Figure 9(a) shows one staring image. This is a midwave IR image of a hanger at the Wright-Patterson Air Force Museum. Pixel replication has been used to produce a 256×256 image to facilitate comparison with the reconstructed microscanned image.

Six blocks of size 10×10 have been used in the BMA to obtain the shift estimates. Bilinear interpolation has been executed on the blocks to estimate the interpixel values, thus allowing for subpixel shift estimates. Table 4 shows the results of the block matching algorithm. The expected shift in the horizontal and vertical directions, as programmed into the microscan system, is listed in the first row and first column respectively. The percentage error of the estimated shift for

Table 4 Motion estimation results (values are percentage errors of the pixel).

n \ m	0.00	0.25	0.50	0.75
0.00	(0, 0)	(0, 0)	(0, 12.5)	(0, 0)
0.25	(12.5, 0)	(12.5, 0)	(12.5, 12.5)	(12.5, 0)
0.50	(20.85, 0)	(18.75, 0)	(18.75, 12.5)	(18.75, 0)
0.75	(2.08, 0)	(2.08, 0)	(4.17, 12.5)	(8.33, 0)

each position is provided in Table 4. These errors are computed with respect to the programmed mirror shifts.

Since accurate subpixel shift estimates are the key to good performance, the BMA has been tested as the noise in the image is increased. Since the imagery is real FLIR imagery, a noise floor is already present. Additional white Gaussian noise has been added to the images. The plot in Fig. 8 shows the percentage error in both the horizontal and vertical directions as a function of the additive noise level. As can be seen, the BMA performs well until the noise reaches a variance of just over 200 ADUs (analog-digital units). Beyond that, the percentage error tends to fluctuate. This may be due to the block selection process. Note that the image variance in this example is 3059 ADUs.

4.3 *High-Resolution Reconstruction*

The image reconstructed using the estimated shifts from the BMA is shown in Fig. 9(b). The BMA and reconstruction algorithms have been implemented on these images using no *a priori* information about the preprogrammed shifts. Each of the 16 staring images has been placed in its bin according to the BMA estimates. Multiple frames placed in the same bin have been averaged. Any empty bins have been filled using a nearest-neighbor interpolation. Ties have been resolved by selecting the pixel value directly above the empty bin. If an empty bin occurred in the first row of the high-resolution grid, it has been filled with the pixel value directly to its left. Notice the improvement in resolution in Fig. 9(b). In Fig. 9(a), neither the row of pine trees across the center of the image nor the rockets behind them are distinguishable. In the high-resolution reconstructed image these objects become identifiable. Furthermore, the "blockiness" seen in Fig. 9(a) is significantly reduced in Fig. 9(b).

5 Conclusions

It is shown here that microscanning is a viable procedure for reducing the aliased energy in staring array imagery. Controlled microscanning generates a uniform high-resolution sampling grid. There are instances, however, when a uniform sampling lattice is not available due to unwanted platform vibration. In addition, one may have an image sequence with subpixel shifts due only to random motion (obtained with no microscan mirror). In these cases, the uncontrolled microscanning technique can be used to reconstruct a high-resolution image from multiple undersampled image frames. The algorithms proposed here are computationally simple, and since many imagers can collect scene data at a more rapid rate than a display can operate, they can be utilized in real time. By exploiting these additional frames, image quality can be significantly improved.

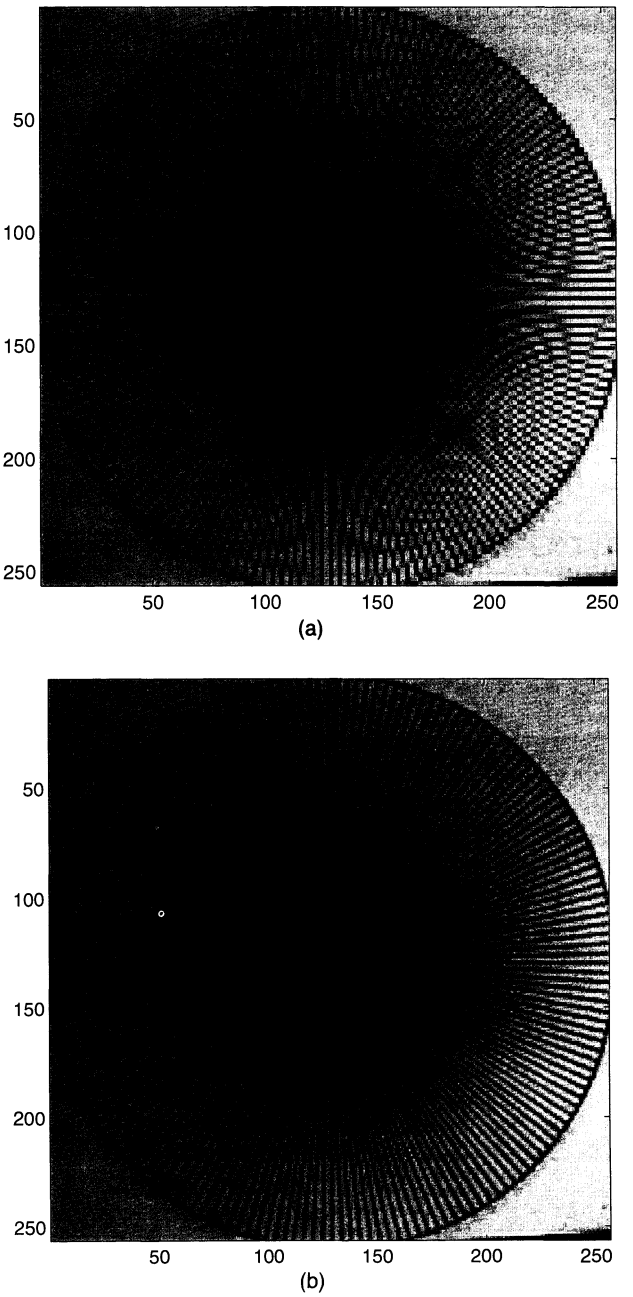

Fig. 7 Spoke-target comparison. Image (a) is a staring image, and image (b) is a level-2 microscan of the same target. Pixel replication has been applied to the staring image to facilitate a comparison.

Acknowledgments

This work was supported under Air Force contract F33601-95-D-J010. The University of Dayton Electrical Engineering and Electro-Optics Departments and Wright Laboratory, Electro-Optics branch (WL/AARI-3), provided the materials and environment to write this paper.

The following people we would like to thank specifically: Bob Muse, Mike Shelton, Joe Richardson, Bob Gualtieri, Tony Absi, Brian Yasuda, Ernie Armstrong, John Bognar, Dr. Mohammed Karim, Dr. Ed Watson, Dr. Paul McManamon, Jim Stewart, and Don Tomlinson. We are very grateful for their support and assistance.

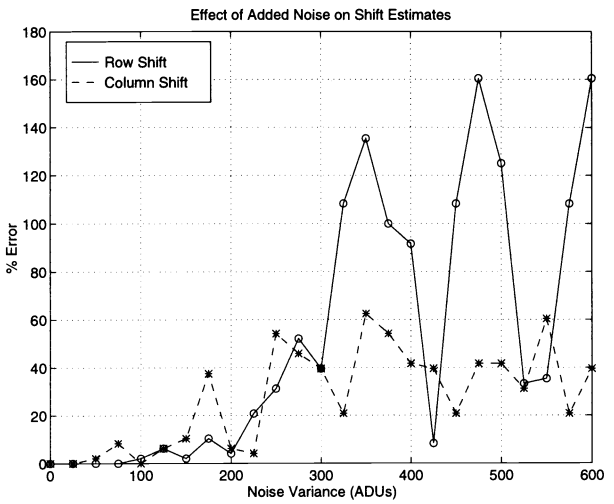

Fig. 8 Effect of additional noise on the BMA shift estimate. Variance of the reference image is 3059 ADUs.

References

1. E. A. Watson, R. A. Muse, and F. P. Blommel, "Aliasing and blurring in microscanned imagery," *Proc. SPIE* **1689,** 242–250 (1992).
2. S. P. Kim, N. K. Bose, and H. M. Valenzuela, "Recursive reconstruction of high resolution image from noisy undersampled multiframes," *IEEE Trans. Acoust. Speech Signal Process.* **38**(6), 1013–1027 (June 1990).
3. J. W. Goodman, *Introduction to Fourier Optics,* McGraw-Hill, New York (1968).
4. E. L. O'Neill, "Transfer function for annular aperture," *J. Opt. Soc. Am.* **46**(4), 285–288 (Apr. 1956).
5. W. K. Pratt, *Digital Image Processing,* pp. 267–285, Wiley, New York (1991).
6. A. K. Jain, *Fundamentals of Digital Image Processing,* Prentice-Hall, Englewood Cliffs, NJ (1989).
7. S. Gupta and A. Gersho, "On fractional pixel motion estimation," *Proc. SPIE* **2094,** 408–419 (1993).
8. J. R. Bergen, P. J. Burt, R. Hingorani, and S. Peleg, "A new motion estimation algorithm," *IEEE Trans. Pattern Anal. and Mach. Intell.* **14**(9), 886–896 (Sep. 1992).
9. E. A. Watson, R. A. Muse, and F. P. Blommel, "Electro-optic systems research using the variable parameter FLIR," in *Proc. IEEE NAECON,* Vol. 3, 1992, pp. 1263–1267.
10. J. D. Gaskill, *Linear Systems, Fourier Transforms and Optics,* pp. 267–285, Wiley, New York (1978).

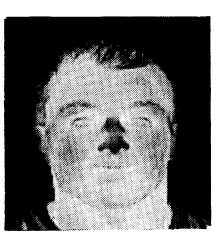

Joseph C. Gillette is currently a research assistant at the University of Dayton. He received a BS degree in electrical engineering from the University of Dayton in 1992 and an MSEE degree in 1994. He is currently working toward his PhD at the University of Dayton. He is conducting research at Wright-Patterson Air Force Base under a contract with Technology/Scientific Services Inc. His research interests include image sequence processing, image processing, microscanning, and other sampling techniques.

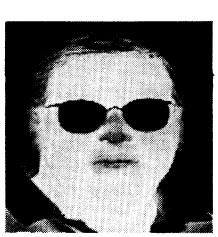

Thomas M. Stadtmiller received a BS degree in applied physics from Xavier University in Cincinnati in 1993. He is currently working toward his MS in electro-optics at the University of Dayton in Dayton, Ohio. As a graduate student, he is conducting research for Technology/ Scientific Services Inc. as a subcontractor at Wright-Patterson Air Force Base in Dayton. His research interests include image processing, motion estimation, and microscan techniques.

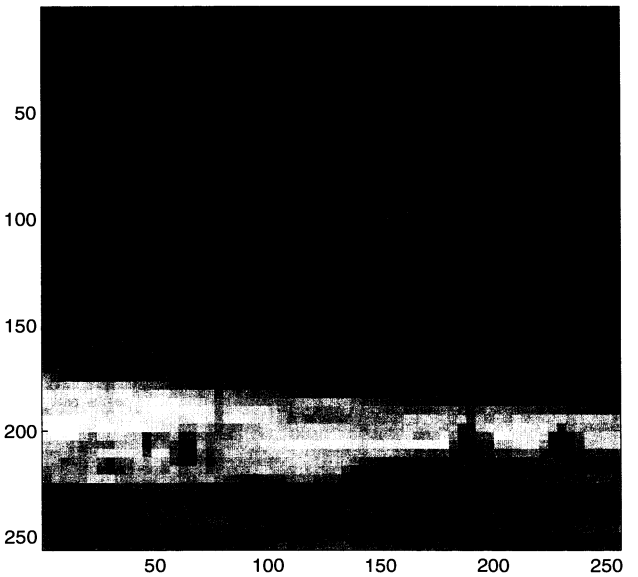

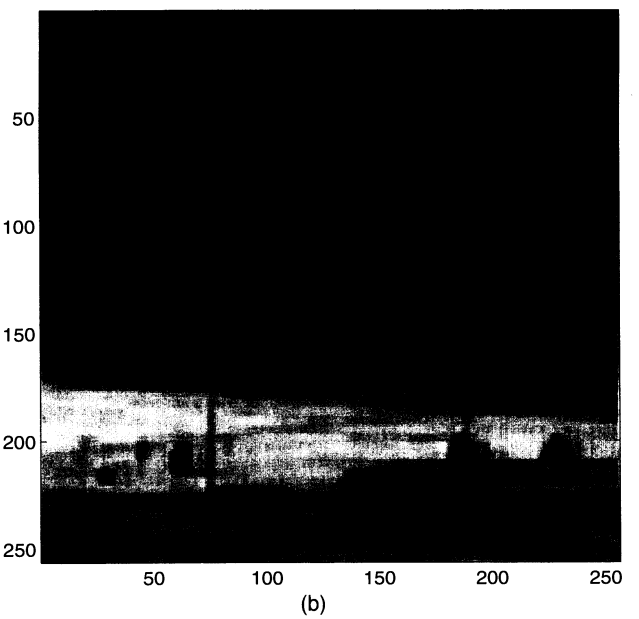

Fig. 9 (a) Staring 64×64 image of the museum of WPAFB. Pixel replication was used to produce the 256×256 image. (b) High-resolution reconstruction using 16 shifted frames.

Russell C. Hardie graduated *magna cum laude* from Loyola College in Baltimore in 1988 with a BS degree. He obtained a MS degree in electrical engineering from the University of Delaware in 1990. In 1992, he obtained a PhD in electrical engineering from the University of Delaware. Dr. Hardie is currently an assistant professor in the Department of Electrical Engineering at the University of Dayton. Prior to teaching at the University of Dayton, Dr. Hardie was a senior scientist at Earth Satellite Corporation (EarthSat) in Rockville, Maryland. He now acts as a consultant to EarthSat developing algorithms for multispectral and hyperspectral image processing. His research interests include signal and image processing, nonlinear filters, adaptive filter theory, pattern recognition, and remote sensing.